Preprint typeset in JINST style - HYPER VERSION

In situ calibration of the single photoelectron charge response of the IceCube photomultipliers

IceCube author list to be inserted... E-mail: analyses@icecube.wisc.edu

ABSTRACT: This technical report outlines the in situ calibration of the single photoelectron charge distributions for each of the Hamamatsu Photonics R7081-02 photomultipliers in the IceCube Neutrino Observatory. We discuss the single photoelectron identification procedure, how we extract the single photoelectron charge distribution using a deconvolution the multi-photoelectron charge distribution, and examine various correlations between the shape of the single photoelectron charge distribution and various hardware components. The time dependence of the charge distributions is also investigated.
Definitions:

1. Charge: WaveDeform fits the waveform with an SPE pulses template. The integral of the fitted pulse, divided by the load resistance, divided by the gain, is the reported measured *charge* of the pulse. It is reported in units of a single electron.
2. PE: The unit of charge. This represents the charge relative to one electron.
3. 1PE: The HV on each DOM is set such that the gain on the PMT is 10^7. It is determined to be at the proper gain (10^7), when the Gaussian mean of the fitted charge distribution is at 1PE.
4. Photoelectron: The physical electron emitted from the photocathode.
5. SPE: (Single Photoelectron) A single physical electron emitted from the photocathode.
6. MPE: (Multiple Photoelectron): multiple electrons emitted from the photocathode, charges may have been combined.
7. Charge distribution: The distribution of the measured charges. This will include both SPE and MPE events.
8. Single Photoelectron Charge distribution: The hypothetical charge distribution generated by observing a pure sample of single photoelectron.
9. SPE Template: The functional form that is used to fit the charge distribution.

KEYWORDS: IceCube, single photoelectron, charge distribution, PMT.

Contents

1. Introduction

The IceCube Neutrino Observatory [1, 2] is a cubic-kilometer sized array of 5,160 photomultiplier tubes (PMTs) buried in the Antarctic ice sheet designed to observe high-energy neutrinos interacting with the ice [3]. As of 2011, the IceCube collaboration completed the installation of the main IceCube detector consisting of 78 vertical strings of PMT modules, and the low-energy infill, DeepCore, consisting of a more densely arranged array of 8 strings [4]. Each string in the detector contains 60 digital optical modules (DOMs), that house a single PMT each, as well as all required electronics [5]. The DOMs extend from 1450 m to 2450 m below the surface of the ice sheet and are spaced 17 m apart in the IceCube detector, and 7 m apart in the DeepCore detector.

Each DOM consists of a 0.5" thick spherical glass pressure vessel that houses a single down-facing 10" R7081-02 PMT from Hamamatsu Photonics [6]. The PMT is specified for wavelengths ranging from 300 nm to 650 nm, with peak quantum efficiency of 25% near 390 nm. Each PMT is coupled to the glass housing with optical gel and is surrounded by a wire mesh of μ-metal to reduce the effect of the ambient Earth's magnetic field. Then glass housing is transparent to wavelengths 350 nm and above [7].

IceCube has also deployed 399 DOMs with Hamamatsu R7081-02MOD PMTs, which, having a peak quantum efficiency of 34% near 390 nm (36% higher efficiency than the standard DOMs),

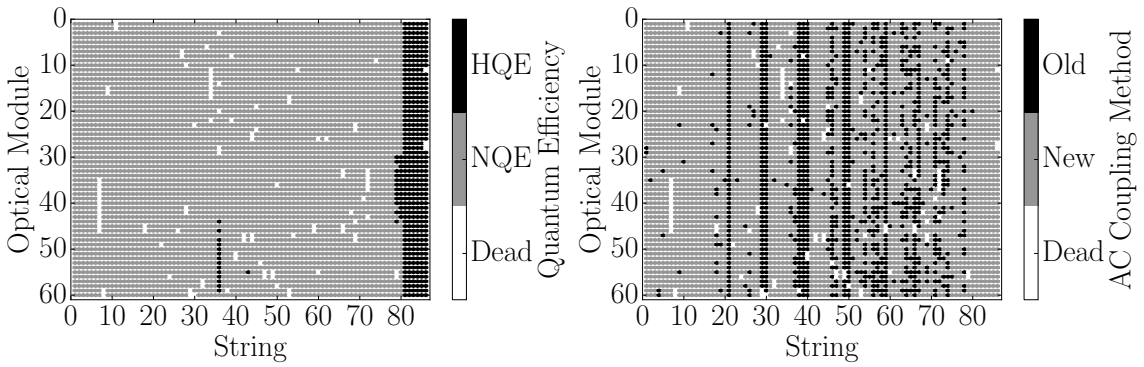

Figure 1. Left: Mapping showing the HQE DOMs (black) and standard normal quantum efficiency (NQE) DOMs (gray). Right: The version of AC coupling, old toroids (black) and new toroids (gray). These figures also show the location of the dead DOMs in white.

are classified as high-quantum efficiency (HQE) DOMs [4]. These DOMs are primarily located in DeepCore, however there are a few located on strings 36 and 43 as well, as shown in the left side of Fig. 1.

The R7081-02 and R7081-02MOD PMTs have 10 dynode stages and are operated with a gain of 10^7 and high voltage around 1200 V (an typical amplified single photoelectron will generate a $\approx$6 mV peak voltage at the input to the front-end amplifiers). The PMTs operate with the anodes at high voltage, therefore the signal is AC coupled to the front-end amplifiers. There are two versions of AC coupling in the detector both of which use custom designed bifilar-wound 1:1 toroidal transformers (the DOM specific AC coupling versions, new and old toroids, are shown in the right side of Fig. 1). The DOMs with the old toroids were designed with an impedance of 43Ω, while the new toroids are 50Ω [8].

IceCube relies on two observables per DOM to reconstruct events: the total number of detected photons and their timing distribution. Both the timing and the number of photons are extracted from the on-board digitized waveforms in software. The waveforms are deconvolved into a series of scaled single photoelectron pulses (so-called pulse-series) and the integral of the individual scaled pulses (divided by the load resistance) defines the observed charge. It will often be expressed in units of PE, or photoelectrons, which further scales the measured charge by the charge of a single electron times the nominal gain (10^7).

When one or more photons produce a charge sufficient to trigger the on-board discriminator (set via a DAC to approximately 0.25PE), the signal acquisition process is triggered. The signal is feed into four parallel input channels. Three of the channels first pass through a 75 ns delay loop in order to capture the leading edge of the pulse, then into three high-speed (300 MSPS for 128 samples) 10-bit waveform digitizers (Analog Transient Waveform Digitizer, ATWD), each of which have a different level of amplification (15.7 ± 0.6, 1.79 ± 0.06, and 0.21 ± 0.01 [8]). There is also three extra ATWDs on-board each DOM: one used for calibration, and the other two operate in a ping-pong fashion to remove dead-time associated with the readout. The signal to the fourth channel is first shaped and amplified, then feed into a 10-bit fast analog-to-digital converter (fADC) operating at a sampling speed of 40 MSPS. Further detail regarding the description of the DOM electronics can be found in Refs. [5, 9].

This technical report is concerned with accurately determining how the individual DOMs collect charge in order to improve calibration and the description of the detector in the Monte Carlo simulation. It describes the procedure used to determine the PMTs gain characteristics as seen in the single photoelectron (SPE) charge distributions using in situ data from the IceCube and DeepCore detectors. The SPE charge distribution refers to the measured charge probability density function of the individual DOMs, generated by the amplification of a pure sample of single photoelectrons. The extraction of the SPE charge distribution was recently made possible by developing a procedure to reduce the multi-photoelectron (MPE) contamination.

1. A specially designed unbiased pulse selection was developed to reduce the MPE contamination while accounting for physical phenomena (e.g. late pulses, afterpulses, pre-pulses, and baseline shifts) and software related effects (e.g. pulse splitting). This will be further described in Sec. 2.1.

2. A fitting procedure that separates the remaining MPE contamination from the SPE charge distribution by deconvolving the measured charged distribution. This is elaborated on in Sec. 2.3.

In using in situ data to determine the SPE charge distributions, we accurately represent the individual PMT response as a function of time, environmental conditions, software version, hardware differences, and sample photons uniformly over the surface of the photocathode. This is beneficial since it also allows us to inspect the stability and long term behavior of the individual DOMs, verify previous calibration, and correlate features and environment to DOM behavior.

1.1 Single photoelectron charge distributions

In an idealized scenario, a single photon produces a single photoelectron, which is then amplified by a known amount and the measured charge corresponds to 1PE. However, there are many physical processes which create structure in the measured charge distributions. For example:

- **Statistical fluctuation due to cascade multiplication** [10]. At every stage of dynode amplification, there is a stochastic spread in the number of emitted electrons that make it to the next dynode. This in turn causes a spread in the measured charge after the gain stage of the PMT.

- **Photoelectron trajectory**. Some electrons may deviate from the favorable trajectory, reducing the number of secondaries produced at a dynode or the efficiency to collect them on the following dynode. This can occur at any stage, however, it has the largest effect on the multiplication at the first dynode [11]. The trajectory of a photoelectron striking the first dynode will depend on many things, include where on the photocathode it was emitted, the uniformity of the electric field, the size and shape of the dynodes [10], and the ambient magnetic field [12, 13].

- **Late or delayed pulses**. A photoelectron can elastically or in-elastically scatter off the first dynode. The scattered electron can then be re-accelerated to the dynode, creating a second pulse. The difference in time between the initial pulse and the re-accelerated pulse in the

R7081-02 PMT was previously measured to be up to 70 ns [7, 14]. The two sub-pulses have lower chargers, but the sum of the two tends to add up to the original charge. Collecting either the initial pulse or the late pulse will result in the charge being reconstructed as lower [15].

- **Afterpulses**. When a photoelectron or the secondary electrons produced during the electron cascade gain sufficient energy to ionize residual gas in the PMT, the positively charged ionized gas will be accelerated in the electric field towards the cathode. Upon impact with the photocathode, electrons can be again released from the photocathode, creating what is called an afterpulse. For the R7081-02 PMTs, the timescale for afterpulses was measured to occur from 0.3 to 11 μs after the initial pulse, with the first prominent afterpulse peak occurring at approximately 600 ns [7]. The spread in the afterpulse time is dependent on the position of photocathode, the charge to mass ratio of the ion produced, and the electric potential distribution [16]; whereas the size of the afterpulse is related to the momentum and species of the ionized gas and composition of the photocathode [17].

- **Pre-pulses**. If an incident photon passes through the photocathode without interaction and strikes one of the dynodes, it can eject an electron that is only amplified by the subsequent stages, resulting in a lower measured charge (lower by a factor of approximately 25). For the IceCube PMTs, the pre-pulses were found to arrive approximately 30 ns before the signal from other photoelectrons from the photocathode [7].

- **Multi-PE contamination**. When multiple photoelectrons arrive at the first dynodes within several nanoseconds of each other, they can be reconstructed by the software as a single, multi-PE pulse.

- **Electronic noise**. This refers to the fluctuations in the analog-to-digital converters (ATWDs and FADC) and ringing arising from the electronics.

Beyond the physical phenomena above that modify the measured charge distribution, there is also a lower limit to the smallest charge that can be extracted. For IceCube, the discriminator limits the trigger pulse to be above 0.25PE, and subsequent pulses in the readout time window are subject to a software defined threshold. The software threshold was set conservatively to avoid extracting pulses that originated from electronic noise. This threshold can be modified to gain access to lower charge pulses, and will be discussed in Sec. 2.2.

The previous model used to describe the SPE charge distribution (known as the TA0003 distribution) represented the above effects as the sum of an exponential plus a Gaussian, where the exponential represented charge of poorly amplified pulses, and the Gaussian represented the spread in statistical fluctuations due to the cascade multiplication. A description of the TA0003 model can be found in Ref. [7]), and the average distribution was previously used to describe all the PMTs in the IceCube and DeepCore detectors.

Recently, IceCube has performed several lab measurements using the R7081-02 PMTs with in-time laser pulses, demonstrating that the in-time charge distribution includes a steeply falling low-charge component below the discriminator threshold. To account for this, a new functional form including a second exponential was introduced. This form of the charge distribution, $f(q)_{SPE} = Exp_1 + Exp_2 +$ Gaussian, is referred to as the *SPE template* in this report. Explicitly:

$$f(q)_{SPE} = E_1 e^{-q/w_1} + E_2 e^{-q/w_2} + N e^{-\frac{(q-\mu)^2}{2\sigma^2}}. \quad (1.1)$$

Where q represents the measured charge; E_1, E_2, and N represent normalization factors of each components; w_1 and w_2 are the exponential decay widths; and μ, σ are the Gaussian mean and width respectively. This is the assumed functional shape of the SPE charge distributions and the components of Eq. 1.1 are determined in this report for all in-ice DOMs. IceCube defines 1PE as the location of the Gaussian mean (μ) and calibrates the gain on the individual PMTs during the start of each season to meet this definition.

1.2 IceCube datasets and software definitions

The largest contribution to the IceCube trigger rate comes from down-going muons produced in cosmic ray induced showers [18]. Cosmic ray muons stopping in the detector cause the individual trigger rate to decrease at lower depths. Further, during the formation of this ice sheet, there have been several periods of colder climate that have caused different optical properties in the ice at different depths. The optical properties also affect the trigger rate, in particular, the “dust layer" from 2100 to 2200 m (optical modules 32-38 in the IceCube detector) below the surface is a region in the ice with a relatively large scattering and absorption coefficient.

An induced signal in the PMT will pass through the AC coupling toroid located on the base of the PMT, then be compared to a discriminator threshold set to 0.25PE. If two adjacent DOMs observe a passing of the discriminator, a *Hard Local Coincidence* (HLC) is initiated and the corresponding waveforms are sampled 128 times and readout on the three ATWDs.

After waveform digitization, there is a correction applied to remove any DC baseline offset and correct for the signal droop and undershoot introduced by either version of the AC coupling. Scaled SPE pulse templates (that take into account the version of the AC coupling) are then fit to the waveforms using software referred to as WaveDeform, which determines the individual pulse time stamp and charge, and populates a pulse series.

The pulse series used in this analysis come from two datasets provided by IceCube:

1. The **MinBias dataset.** This dataset records the full waveform readout of randomly triggered HLC events, at a rate that corresponds on average to 1/1000 events. The largest contribution to the IceCube trigger rate comes from down-going muons produced in cosmic ray induced showers [18] and therefore is the largest signal component in this dataset. The full waveform of these events allows us to extract the raw information about the individual pulses and therefore, this will be used to measure the individual PMT charge distributions.

2. The **BeaconLaunch dataset.** This is a forced-trigger (not triggered by the discriminator) filter that is typically used to monitor the individual DOM baseline. It therefore also includes the full ATWD window waveform readout. Since this dataset is forced-triggered, the majority of these waveforms represent baseline fluctuations, however there will be the occasional coincidental pulse that makes it into the readout window. This dataset will be used to examine the noise contribution to the charge distributions. Note: when using this datasets, the weight of every pulse is scaled by a factor of 28.4 to account for the livetime difference between the MinBias dataset and the BeaconLaunch dataset.

This analysis uses the full MinBias and BeaconLaunch datasets from IceCube season 2011 to 2016 (subsequently referred to as IC86.2011 to IC86.2016). Seasons in IceCube typically start in June of the labeled year and end approximately one year later. Calibration is performed at the beginning of each season.

2. Extracting the SPE templates

2.1 Single photoelectron pulse selection

The pulse selection is the method used to extract candidate, unbiased, single photoelectron pulses from data, while minimizing the multi-PE contamination. It avoids collecting afterpulses, rejects late pulses from the trigger, reassembles late pulses, accounts for the discriminator threshold, reduces the effect of droop and baseline undershoot, and gives sufficient statistics to perform a season-to-season measurement. An illustrative diagram of the pulse selection is shown in the left side of Fig. 2, while a description of the procedure is detailed below.

In order to trigger a DOM, the input to the front-end amplifiers must exceed the discriminator threshold. To avoid the selection bias of the discriminator trigger, we ignore the trigger pulse as well as the entire first 100 ns of the time window. Ignoring the first 100 ns has the added benefit of also removing late pulses that could be attributed to the triggering pulse. To ensure we are not accepting afterpulses into the selection, we also enforce that the pulse of interest (POI) is within the first 325 ns of the ATWD time window. In the vicinity of the POI, we check that WaveDeform did not reconstruct any pulses up to 50 ns prior to the POI, or 100-150 ns after the POI (the light-gray

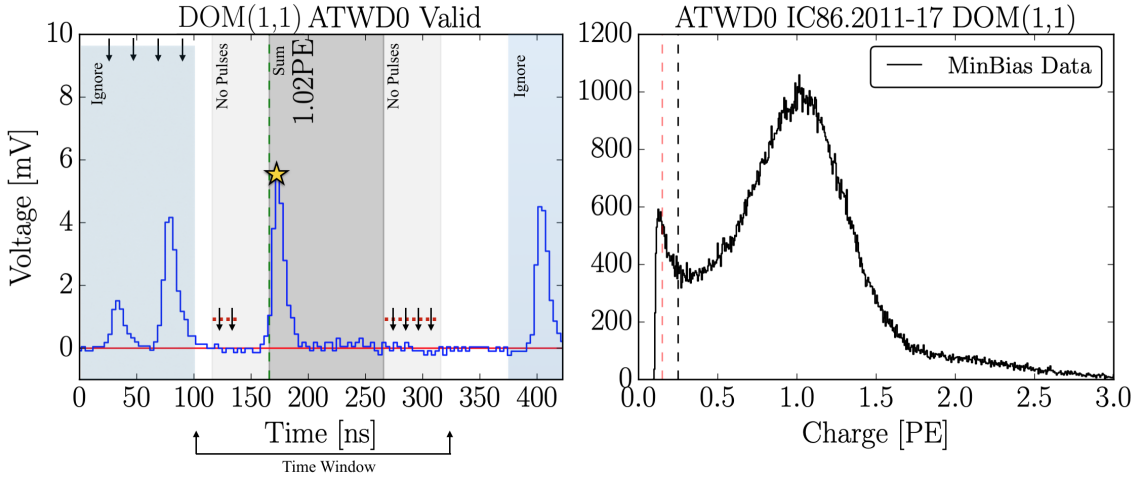

Figure 2. Left: An illustrative diagram of the pulse selection criteria for a selecting a high purity and unbiased sample of single photoelectrons. The pulse of interest is identified with the yellow star. We see a small trigger pulse at 25 ns (due to the delay board), followed by a potential late pulse. At 400 ns, we see a pulse in the region susceptible to afterpulses. Right: the collected charges from string 1, optical module 1 (DOM 1,1), from the MinBias data collected from IC86.2011 to IC86.2016 using the pulse selection. The discriminator threshold at 0.25PE is shown as a dotted black vertical line. For visual purposes, a dotted-red line is also included at 0.15PE.

region of Fig. 2 Left). This later constraint is to reduce the probability of accidentally splitting a late pulse in the summation window.

Restrictions are put on the full ATWD waveforms as well, such as ensuring that the trigger pulse does not exceed 10 mV (to reduce the effect of the subsequent baseline undershoot due to the AC coupling or other artifacts from large pulses) as well as a global constraint that the time window cannot contain any pulses that exceeds 20 mV.

If a pulse is reconstructed between 100 and 325 ns after the time window is opened and the voltage criteria is met, it is accepted as a candidate photoelectron and several checks are performed on the waveform prior-to and after the pulse. The first check is to ensure that the waveform is near the baseline just prior to the rising edge of the POI. This is accomplished by ensuring that the waveform does not exceed 1 mV, 50 to 20 ns prior to the POI, and eliminates cases where the POI is a late pulse. We also ensure the waveform returns to the baseline by checking that no ADC measurement exceeds 1 mV, 100 to 150 ns after the POI (these constraints are illustrated as the red-dotted lines and black arrows in Fig. 2 Left).

If all the above criteria are met, we sum the reconstructed charges from the POI time (given by WaveDeform) to +100 ns (the dark gray area of in Fig. 2 Left). This ensures that any nearby pulses are either fully separated or fully added (in-case WaveDeform incorrectly split the pulse, and to reassemble late pulses). The 100 ns summation also means that the pulse selection we will occasionally be accepting MPE events.

2.2 Characterizing the low-charge region

Fig. 2 (right) shows the charge distribution in black of the selected pulses that pass the single photoelectron pulse selection for string 1, optical module 1 (DOM (1,1)). In the low-charge region (below 0.25PE), we see a steep rise (in agreement with the in-time laser tests mentioned in Sec. 1.1), then a second threshold at approximately 0.13PE. This is a software defined threshold that comes from WaveDeform not attempting to deconvolve charges smaller than a predefined size. The threshold was set to avoid electronic noise being interpreted as PMT pulses and contaminating the low-charge region. This section will examine the effect on the charge distribution and noise contribution by lowering the WaveDeform threshold. The aim will be to explore the low-charge region.

Fig. 3 (left) shows the charge distributions for the MinBias (black) and the BeaconLaunch (red) datasets using the default settings on WaveDeform. As mentioned in Sec. 1.2, occasionally a photoelectron will be coincident with the forced BeaconLaunch time window and populate a single photoelectron distribution. Subtracting the shape of the MinBias charge distribution from the BeaconLaunch dataset yields an estimate of the amount of electronic noise contamination (blue). The bin with the largest signal-to-noise ratio (SNR) above 0.1PE was found to have 0.0013. The SNR for the the full distribution was found to be 0.0005. Fig. 3 (right) shows the same data after lowering the WaveDeform threshold. Correspondingly, the bin with the largest SNR was found to be 0.0017, whereas the total SNR was found to be 0.0015.

2.3 Fitting procedure

The fit assumes that there is a negligible three-PE contribution, which is justified by the lack of statistics in the 3PE region as well as the significant scale difference between the 1PE and 2PE

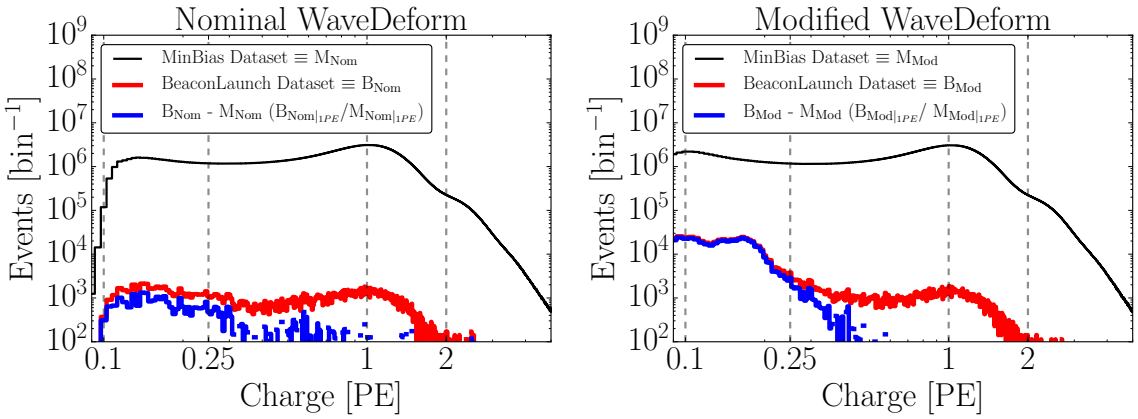

Figure 3. The cumulative charge distributions (IC86.2011-2016) of all DOMs for the MinBias and BeaconLaunch datasets. The blue histogram shows the expected contribution from noise (found by subtracting the shape of the MinBias dataset from the BeaconLaunch dataset). Left: The charge distributions for the standard WaveDeform settings. Right: The charge distributions for the modified WaveDeform settings.

region, as shown in Fig. 2 (right). The 2PE charge distribution is assumed to the be SPE charge distribution convolved with itself [19]. A python-based piece of software called the "convolutional fitter" is used to determine the components of Eq. 1.1 from the measured charge distribution that includes the multi-PE contamination.

The Exp_2 component (as well as the Exp_1) of Eq. 1.1, represents poorly amplified photoelectrons and therefore we do not allow it to extend beyond the high charge region of the Gaussian component. In particular, we include a constraint on the the parameter w_2 to ensure that it falls off with the Gaussian component:

$$w_2 < \frac{\mu + 2\sigma}{4 - \text{Ln}(N/E_2)}. \tag{2.1}$$

This equation was found by setting the Exp_2 to be $1/e^2$ that of the Gaussian component at two sigma (the Exp_1 is neglected from this equation since it falls off in the low-charge region). Eq. 2.1 is used as a constraint during the fit to the charge distributions.

Pulses that fall below the WaveDeform threshold and are not reconstructed contribute to an effective efficiency of the individual DOMs. This analysis assumes the same shape of the steeply falling exponential component (Exp_1) for all DOMs in the detector to avoid large fluctuations in the individual DOM efficiencies. The modified WaveDeform data will strictly be used to determining the average low-charge region. Specifically, we will fit the cumulative charge distribution to determine the components of Eq. 2.1 with the modified WaveDeform, background subtract the BeaconLaunch data, and only use the measured shape and normalization of Exp_1 in all subsequent non-modified WaveDeform fits.

The Exp_1 component is inserted into the non-modified WaveDeform fits and the SPE templates are extracted. The residual of the fit compared to data is calculated and expressed as a percentage difference. The average residual of all DOMs is then calculated and used as global scaling factor for all SPE templates.

Failed fits (DOMs removed from service (109 DOMs) and DOMs that fail any one of several validity checks on the goodness of fit (6 DOMs)) are not included in this report, however, in the MC software chain they are assigned the AVG charge distribution.

2.4 SPE template fit results

Using the background subtracted modified WaveDeform dataset, the steeply falling exponential component was determined by fitting from 0.1PE to 3.5PE to be $E_1 = 6.9 \pm 1.5$ and $w_1 = 0.032 \pm 0.002$PE. The shape of the steeply falling exponential is then used to describe the low-PE charge region for all subsequent non-modified WaveDeform fits.

Using the non-modified WaveDeform dataset with the value for E_1 described above, the SPE templates are extracted for every DOM, separately for each IceCube season (IC86.2011 to IC86.2016). An average fit was also performed in which all the data was summed together (labeled as "AVG"). The fit range for Exp_2 and the Gaussian components are selected to be between 0.15PE and 3.5PE. The average residual for all DOMs from 0 to 1PE is shown in Fig. 4.

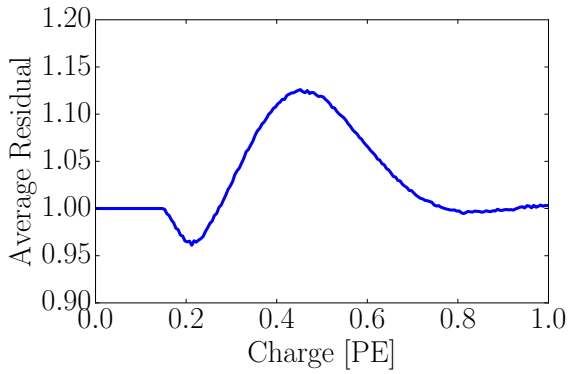

Figure 4. The measured average residual of the SPE templates fit.

An example fit is shown in Fig. 5 for the cumulative charge distribution for DOM (1,1). The collected charge distribution is shown in the black histogram, while the convolutional fit is shown as the black line (scaled by the residual). The extracted SPE template (also scaled by the residual) for this DOM is shown in red. The 2PE component from the fit is shown in blue.

The mean value and 1σ spread of the fit parameters, excluding Exp_1, for the IceCube and DeepCore detectors are shown in Table 1 and Table 2 respectively.

The individual DOM SPE templates were then examined between IceCube seasons for a time dependence on the fit parameters. For every DOM, the change over time of each fit parameter (excluding Exp_1) was calculated.

Fig. 6 shows the change in a given fit parameter (represented in percentage deviation from the mean value), per year, of each DOM in both the IceCube (left) and DeepCore (right) detectors. The spread in the fit parameters were found to be consistent with statistically scrambling the yearly measurements. All the fit parameters are found to deviate less than 0.1% per year in both detectors, which is in agreement with the stability checks performed in Ref. [8].

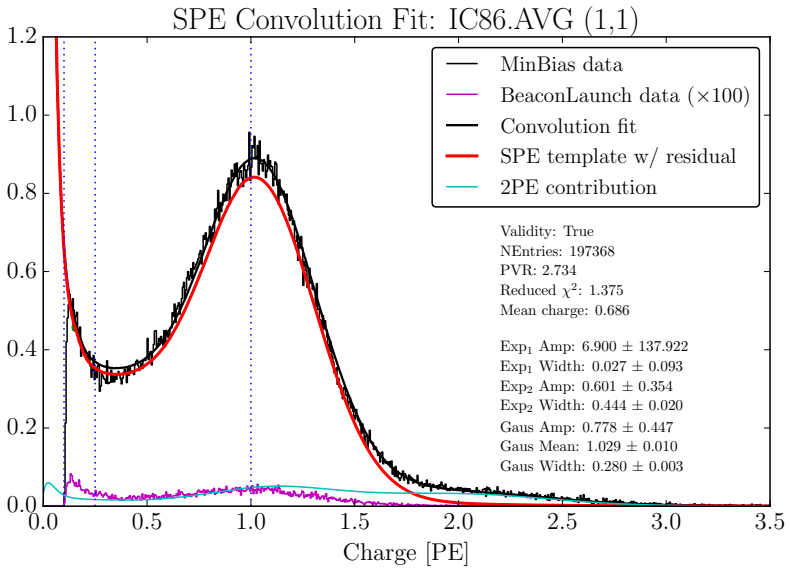

Figure 5. An example fit result for DOM (1,1) using the non-modified WaveDeform dataset from all seasons. The result from the convolutional fitter is shown in black. The extracted SPE template is shown in red. The purple histogram is the full detector (all DOMs summed together) non-modified BeaconLaunch dataset, scaled to the livetime of the MinBias data and further multiplied by a factor of 100 in order to be visible on this plot.

IceCube	Exp_2 Amplitude	Exp_2 Width	Gaus. Amplitude	Gaus. Mean	Gaus. Width
IC86.2011	0.601 ± 0.101	0.457 ± 0.070	0.736 ± 0.061	1.022 ± 0.030	0.296 ± 0.033
IC86.2012	0.595 ± 0.100	0.462 ± 0.065	0.740 ± 0.062	1.020 ± 0.034	0.295 ± 0.033
IC86.2013	0.602 ± 0.101	0.452 ± 0.071	0.736 ± 0.060	1.021 ± 0.033	0.298 ± 0.032
IC86.2014	0.597 ± 0.099	0.453 ± 0.071	0.736 ± 0.059	1.019 ± 0.030	0.299 ± 0.030
IC86.2015	0.604 ± 0.099	0.457 ± 0.067	0.735 ± 0.061	1.024 ± 0.032	0.296 ± 0.032
IC86.2016	0.600 ± 0.101	0.460 ± 0.063	0.736 ± 0.060	1.024 ± 0.030	0.295 ± 0.031

Table 1. The average fit value and 1σ spread for the IceCube detector. The active DOMs in the IceCube detector are 99.4% normal quantum efficiency and 31.0% of the DOM have the original method of AC coupling. Correspondingly, there are 0.6% HQE DOMs and 69.0% of the DOM have the new version of AC coupling.

3. Discussion

3.1 Correlations between fit parameters and DOM hardware differences

As noted in Sec. 1, there are two DOM-related hardware differences: the subset of HQE DOMs and the version of AC coupling used to couple the signal from the PMT anode to the front-end amplifiers. Correlations between the different hardware configurations were examined for correlations with the SPE template fit components.

The HQE DOMs were found to have a larger Exp_2 component (2.3% lower w_2 component,

DeepCore	Exp_2 Amplitude	Exp_2 Width	Gaus. Amplitude	Gaus. Mean	Gaus. Width
IC86.2011	0.519 ± 0.095	0.462 ± 0.099	0.763 ± 0.073	1.023 ± 0.031	0.307 ± 0.038
IC86.2012	0.517 ± 0.095	0.467 ± 0.098	0.763 ± 0.074	1.024 ± 0.032	0.306 ± 0.038
IC86.2013	0.520 ± 0.092	0.461 ± 0.096	0.763 ± 0.073	1.024 ± 0.030	0.306 ± 0.037
IC86.2014	0.522 ± 0.093	0.459 ± 0.098	0.765 ± 0.073	1.021 ± 0.031	0.306 ± 0.038
IC86.2015	0.525 ± 0.095	0.458 ± 0.099	0.763 ± 0.072	1.023 ± 0.031	0.307 ± 0.038
IC86.2016	0.522 ± 0.095	0.464 ± 0.098	0.763 ± 0.074	1.024 ± 0.031	0.305 ± 0.038

Table 2. The average fit value and 1σ spread for the DeepCore detector. The active DOMs in DeepCore are 12.4% NQE DOMs and 0.2% of the DOM have the original method of AC coupling. Correspondingly, the DeepCore contains 87.6% HQE DOMs and 99.8% of the DOM have the new version of AC coupling.

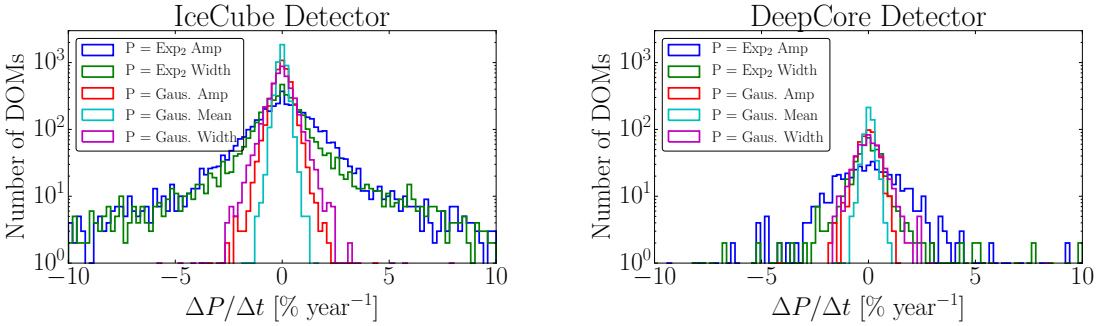

Figure 6. The change in individual DOM fitted parameters over time (Left: IceCube, Right: DeepCore). The change in the fit value is represented in percentage deviation from the mean fit parameter value.

and a 19.9% higher E_2, described in terms of Eq.1.1) than the standard DOMs[1]. Consequently, the HQE DOMs have an 14.9% lower peak-to-valley ratio and a 3.3% lower mean charge. These distributions are shown in Fig. 7.

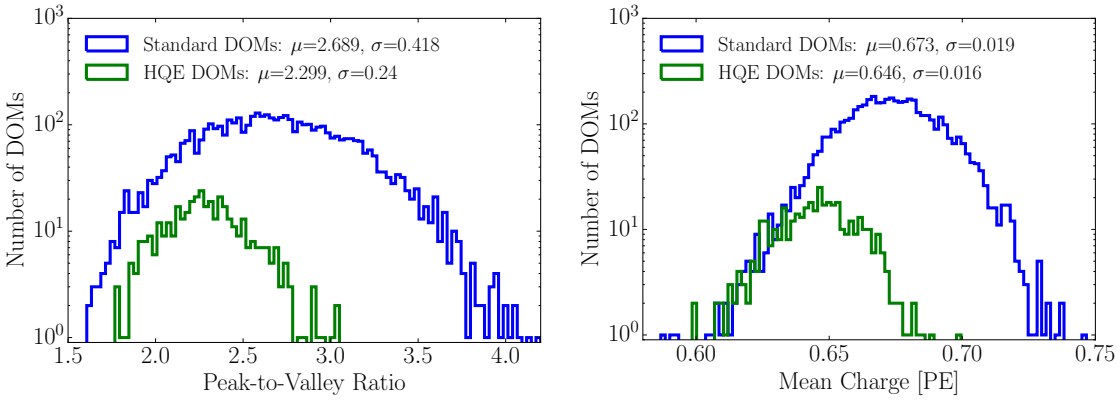

Figure 7. Comparison between the R7081-02MOD HQE DOMs and standard R7081-02 DOMs. Left: The Peak-to-Valley ratio for the two subsets of quantum efficiencies. Right: The mean charge of the individual DOM SPE templates.

The subset of NQE DOMs with the original AC coupling transformer were found to have a

[1]This difference is still observed when comparing the DOMs at similar depths in the detector.

6.1% narrower Gaussian width and an 8.0% larger Gaussian amplitude (σ and N in Eq. 1.1). The exponential component Exp_2 was also found to have a 7.5% lower E_2 component, and a 3.0% higher E_2,component. Although the old toroid DOMs were deployed into ice earlier than the new toroid DOMs, the difference above is still noted when examining individual deployment years, therefore the shape differences are not attributed to the change in the DOM behavior over time. However, the DOMs with the old toroids used the first PMTs to be manufactured by Hamamatsu, therefore, this difference may also be attributed to a gradual change in the process parameters over the course of the PMT manufacturing change in the production procedure rather than the actual AC coupling version. (Spencer: I've checked this, if the PMTSerial is sequential with the production date, this is not attributed to manufacturing).

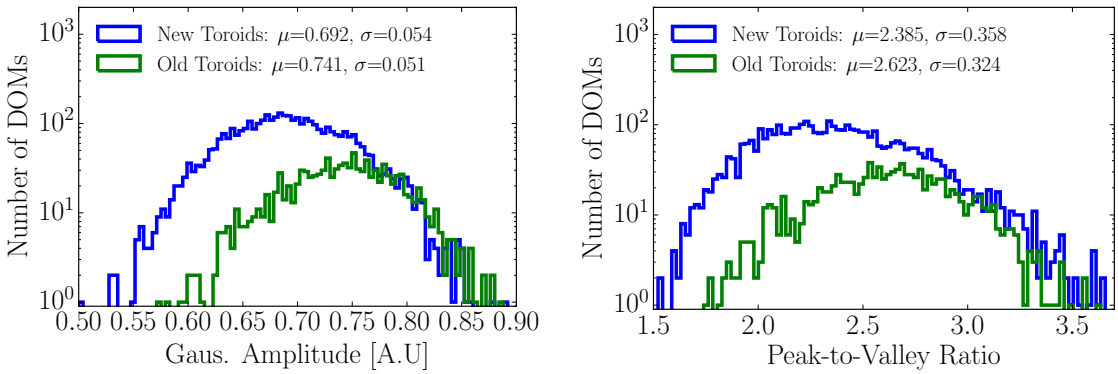

Figure 8. Comparison between the AC coupling version used on the NQE DOMs. Left: The distribution of the measured Gaussian amplitudes. Right: The distribution of the measured Peak-to-Valley ratios.

3.2 Quantifying observable changes when modifying the PMT charge distributions

Changing the assumed gain response in simulation, as deduced from data, has different implications depending on the typical illumination level as present in different analysis. These differences are outlined in the following.

The PMT response is described by a combination of a "bare" efficiency, η_0, and a normalized charge response function, $f(q)$. The bare efficiency represents the fraction of arriving photons that result in any non-zero charge response, including those well below the discriminator threshold. The normalization condition is:

$$\int_0^{\inf} f(q)dq = 1. \tag{3.1}$$

Generally, $f(q)$ and η_0 have to be adjusted together to maintain agreement with a quantity known from lab or in-ice measurements, such as the predicted number of pulses above threshold for a dim source.

Dim source measurements Where light levels are low enough, sub-discriminator pulses do not contribute any observed charge because they do not satisfy the trigger threshold and the probability of two photons arriving together is negligible. Given some independent way of knowing the number of arriving photons, a lab or in-ice measurement determines the trigger fraction above threshold

$\eta_{0.25}$ and/or the average charge over threshold $Q_{0.25}$, either of which can be used to constrain the model as follows:

$$\eta_{0.25} = \eta_0 \int_{0.25q_{pk}}^{\inf} f(q)dq \tag{3.2}$$

$$Q_{0.25} = \eta_0 \int_{0.25q_{pk}}^{\inf} qf(q)dq \tag{3.3}$$

Here, the discriminator threshold is assumed to be 0.25 times the peak position q_{pk}. It is also useful to scale observed charges by q_{pk}, since we set each PMT gain by such a reference, and then a measurement constraint would be stated in terms of $Q_{0.25}/q_{pk}$.

Semi-bright source measurements Once the ATWD window is open, subsequent pulses are not limited by the discriminator threshold, however, WaveDeform introduces a software threshold at 0.1PE (described at the end of Section 2.1). The average charge of an individual pulse that arrive within the time window is therefore:

$$Q_{0.10} = \eta_0 \int_{0.10q_{pk}}^{\inf} qf(q)dq \tag{3.4}$$

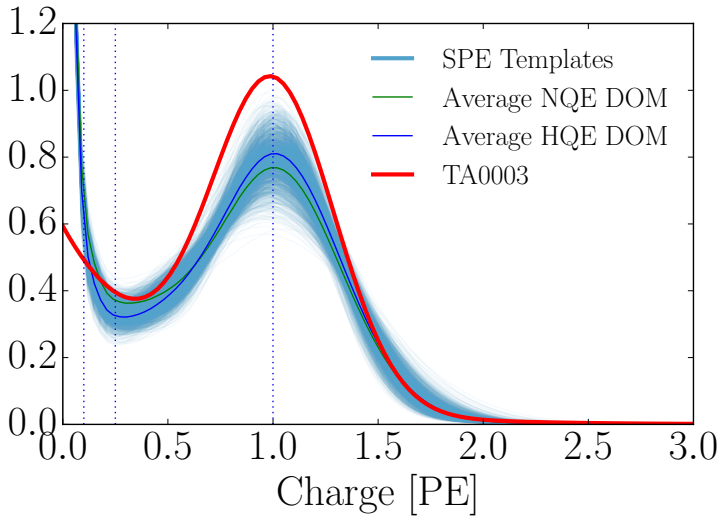

Figure 9. Left: The normalized charge distributions. The TA0003 distribution is shown in red, while the cumulative SPE templates for DOMs in both IceCube and DeepCore are shown in Blue. Right: An analysis level comparison for the TA0003 distribution compared to the SPE Templates to the full data from IC86.2017.

Bright source measurements For light levels that are large, the trigger is satisfied regardless of the response to individual photons, and the total charge per arriving photon therefore includes contributions below both the discriminator and the WaveDeform thresholds:

$$Q_0 = \eta_0 \int_0^{\inf} q f(q) dq \tag{3.5}$$

As such the total charge is directly proportional to the average charge of the SPE template, having a strong dependence on the steeply falling exponential.

3.2.1 Model comparison

When the charge distribution model is changed in a way that preserves agreement with the measured $\eta_{0.25}$ or $Q_{0.25}/q_{pk}$, i.e. η_0 is adjusted properly for changes in $f(q)$, the physical effect can be summarized by the change in the bright-to-dim ratios $Q_0/Q_{0.25}$, and $Q_0/Q_{0.10}$. Conveniently, these ratios depend only on the shape of $f(q)$. Table 3 compares these ratios in terms of the previous charge distribution (TA0003) and the SPE templates described here.

Model	Detector	$Q_0/Q_{0.25}$	$Q_0/Q_{0.10}$	$\eta_{0.25}/Q_{0.25}$
TA0003	IceCube and DeepCore	1.017	1.003	0.969
SPE Templates	IceCube	1.031±0.003	1.013±0.001	0.971±0.006
SPE Templates	DeepCore	1.034±0.002	1.014±0.001	0.965±0.006

Table 3. The distribution in bright-to-dim ratios for the previous charge distribution (TA0003) and the individual DOM SPE templates for the IceCube and DeepCore detector.

Table 3, shows percent-level differences in the physically observable bright-to-dim ratios. Fig. 9 shows the shape difference between the TA0003 distribution and all the SPE templates measured in this report. The shape difference is attributed to a better control of the low-charge region, the difference in functional form (described in Section 1.1), as well as the fact that the SPE templates sample uniformly over the entire photocathode at random incident angles.

3.3 SPE templates in simulation

The IceCube Monte Carlo simulation chain assigns a charge to every photoelectron generated at the surface of the photocathode. The charge is determined by sampling from a normalized charge distribution. A comparison between describing the charge distribution using the SPE templates compared to the TA0003 distribution follows.

Two simulation sets consisting of the same set of events were processed through the IceCube Monte Carlo simulation chain to the final level of the multi-year High Energy Sterile Analysis. At analysis level, the events that pass the cuts are / >99.9% pure up-going (directed upwards relative to the horizon) secondary muons produced by charged current muon neutrino interactions. The energy range of this event selection is between 500GeV-10TeV in reconstructed quantities.

Fig. 10 (left) shows the distribution of the total measured charge in a single DOM during each event. The data is shown for the full IC86.2012 season, but statistically equivalent to any of the other seasons. The simulation set using the TA0003 charge distribution is shown in orange, and the

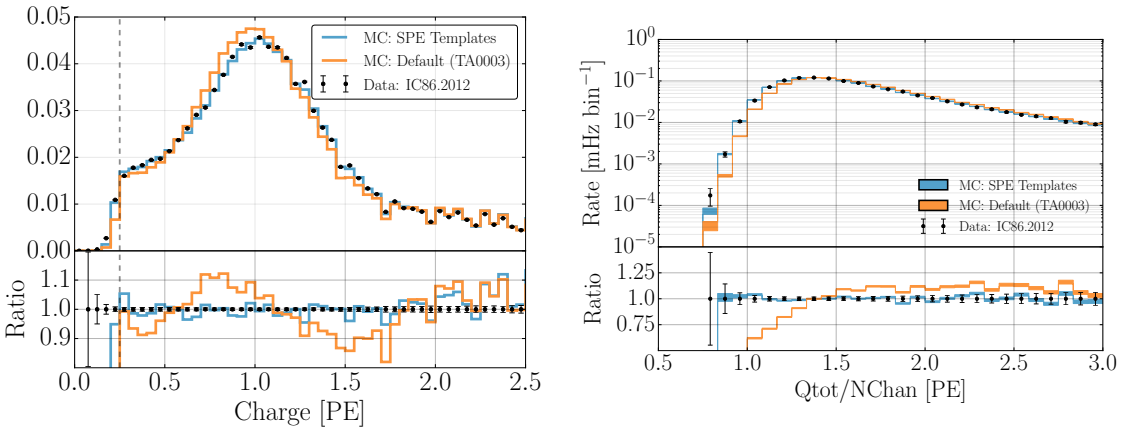

Figure 10. A comparison between the SPE Templates (blue) and the TA0003 (orange) model for describing the SPE charge distribution in Monte Carlo. The simulation is compared to the 2012 IceCube season. Left: The total measured charge per DOM, per event at analysis level. Right: The distribution of the total measured charge of an event divided by the number of DOMs that participated in the event.

SPE Templates is shown in blue. The bottom of the plot shows the ratio of the measured quantity relative to data.

Fig. 10 (right) shows the distribution of the measured total charge on a DOM (after noise removal) divided by the number of channels, or DOMs, that participated in the event.

3.4 SPE templates for calibration

IceCube calibrates the gain setting at the beginning of the season such that the Gaussian mean charge distribution corresponds to a gain of 10^7 (equivalently labelled as 1PE). Since the method used to extract the Gaussian mean described in this report is different from the previous method used for calibration of the DOMs the total measured charge from a DOM is expected to change with the updated calibration.

As shown in Table 1, the Gaussian mean component of the fit of every year is found to be on average 2.2% higher than unity, corresponding to a systematic overestimation of the measured charge in the detector along with a standard deviation of 3.1%. This correction to the measured charge can be implemented by dividing the reported charge from WaveDeform by the corresponding Gaussian mean for a given DOM. This can be done retroactively in IceCube by reprocessing the data (commonly referred to as a "Pass").

4. Conclusion

This report outlines the procedure used for collecting a relatively pure sample of single photoelectron charges for each of the in-ice DOMs in IceCube. Multi-PE contamination was removed using the assumption that the MPE contamination is the convolution of the SPE distribution multiple times.

The SPE templates were extracted for each DOM and each season in the IceCube and DeepCore detectors, and investigated for correlations with hardware related features. Both detectors do not show more than a 0.5% deviation in any of the fitted parameters over the investigated seasons,

in agreement with Ref. [8]. Yearly variations in the fit parameters are consistent with statistical fluctuations. The HQE DOMs located in the IceCube and DeepCore detectors were found to have a distinguishable Exp_2 component from the standard DOMs. Similarly, DOMs with the original method of AC coupling were found to have a narrower and larger Gaussian component. This was not found to be due to a manufacturing process, however is still under investigation.

The SPE templates were implemented into the MC simulation chain and show an improvement in the overall description of charge in the detector. Modern IceCube simulation sets use this update.

The new method for extracting the calibration constant that determines the gain setting on each of the PMTs (the Gaussian mean of the fit), has been revised and shows that the average gain was approximately $2.2\% \pm 3.1\%$ higher than expected.

Acknowledgments

We acknowledge the support from the following agencies: U.S. National Science Foundation - Office of Polar Programs, U.S. National Science Foundation - Physics Division, University of Wisconsin Alumni Research Foundation, the Grid Laboratory Of Wisconsin (GLOW) grid infrastructure at the University of Wisconsin - Madison, the Open Science Grid (OSG) grid infrastructure; U.S. Department of Energy, and National Energy Research Scientific Computing Center, the Louisiana Optical Network Initiative (LONI) grid computing resources; Natural Sciences and Engineering Research Council of Canada, WestGrid and Compute/Calcul Canada; Swedish Research Council, Swedish Polar Research Secretariat, Swedish National Infrastructure for Computing (SNIC), and Knut and Alice Wallenberg Foundation, Sweden; German Ministry for Education and Research (BMBF), Deutsche Forschungsgemeinschaft (DFG), Helmholtz Alliance for Astroparticle Physics (HAP), Research Department of Plasmas with Complex Interactions (Bochum), Germany; Fund for Scientific Research (FNRS-FWO), FWO Odysseus programme, Flanders Institute to encourage scientific and technological research in industry (IWT), Belgian Federal Science Policy Office (Belspo); University of Oxford, United Kingdom; Marsden Fund, New Zealand; Australian Research Council; Japan Society for Promotion of Science (JSPS); the Swiss National Science Foundation (SNSF), Switzerland; National Research Foundation of Korea (NRF); Villum Fonden, Danish National Research Foundation (DNRF), Denmark.

References

[1] J. Ahrens *et al.*, "Icecube preliminary design document," *URL http://www. icecube. wisc. edu/science/publications/pdd*, 2001.

[2] A. Achterberg, M. Ackermann, J. Adams, J. Ahrens, K. Andeen, D. Atlee, J. Baccus, J. Bahcall, X. Bai, B. Baret, *et al.*, "First year performance of the icecube neutrino telescope," *Astroparticle Physics*, vol. 26, no. 3, pp. 155–173, 2006.

[3] I. Collaboration *et al.*, "Evidence for high-energy extraterrestrial neutrinos at the icecube detector," *Science*, vol. 342, no. 6161, p. 1242856, 2013.

[4] R. Abbasi, Y. Abdou, T. Abu-Zayyad, M. Ackermann, J. Adams, J. Aguilar, M. Ahlers, M. Allen, D. Altmann, K. Andeen, *et al.*, "The design and performance of icecube deepcore," *Astroparticle physics*, vol. 35, no. 10, pp. 615–624, 2012.

[5] R. Abbasi, M. Ackermann, J. Adams, M. Ahlers, J. Ahrens, K. Andeen, J. Auffenberg, X. Bai, M. Baker, S. Barwick, *et al.*, "The icecube data acquisition system: Signal capture, digitization, and timestamping," *Nuclear Instruments and Methods in Physics Research Section A: Accelerators, Spectrometers, Detectors and Associated Equipment*, vol. 601, no. 3, pp. 294–316, 2009.

[6] Hamamatsu, "Datasheet."

[7] R. Abbasi, Y. Abdou, T. Abu-Zayyad, J. Adams, J. Aguilar, M. Ahlers, K. Andeen, J. Auffenberg, X. Bai, M. Baker, *et al.*, "Calibration and characterization of the icecube photomultiplier tube," *Nuclear Instruments and Methods in Physics Research Section A: Accelerators, Spectrometers, Detectors and Associated Equipment*, vol. 618, no. 1-3, pp. 139–152, 2010.

[8] M. Aartsen *et al.*, "The icecube neutrino observatory: Instrumentation and online systems, jinst 12 (03)(2017) p03012," *arXiv preprint arXiv:1612.05093*, pp. 1748–0221.

[9] R. Stokstad, "Design and performance of the icecube electronics," 2005.

[10] Hamamatsu, "Basics and applications," Third Edition.

[11] Hamamatsu, "Handbook, chapter 4."

[12] J. Brack, B. Delgado, J. Dhooghe, J. Felde, B. Gookin, S. Grullon, J. Klein, R. Knapik, A. LaTorre, S. Seibert, *et al.*, "Characterization of the hamamatsu r11780 12 in. photomultiplier tube," *Nuclear Instruments and Methods in Physics Research Section A: Accelerators, Spectrometers, Detectors and Associated Equipment*, vol. 712, pp. 162–173, 2013.

[13] E. Calvo, M. Cerrada, C. Fernández-Bedoya, I. Gil-Botella, C. Palomares, I. Rodríguez, F. Toral, and A. Verdugo, "Characterization of large-area photomultipliers under low magnetic fields: Design and performance of the magnetic shielding for the double chooz neutrino experiment," *Nuclear Instruments and Methods in Physics Research Section A: Accelerators, Spectrometers, Detectors and Associated Equipment*, vol. 621, no. 1-3, pp. 222–230, 2010.

[14] F. Kaether and C. Langbrandtner, "Transit time and charge correlations of single photoelectron events in r7081 photomultiplier tubes," *Journal of Instrumentation*, vol. 7, no. 09, p. P09002, 2012.

[15] B. Lubsandorzhiev, P. Pokhil, R. Vasiljev, and A. Wright, "Studies of prepulses and late pulses in the 8" electron tubes series of photomultipliers," *Nuclear Instruments and Methods in Physics Research Section A: Accelerators, Spectrometers, Detectors and Associated Equipment*, vol. 442, no. 1-3, pp. 452–458, 2000.

[16] K. Ma, W. Kang, J. Ahn, S. Choi, Y. Choi, M. Hwang, J. Jang, E. Jeon, K. Joo, H. Kim, *et al.*, "Time and amplitude of afterpulse measured with a large size photomultiplier tube," *Nuclear Instruments and Methods in Physics Research Section A: Accelerators, Spectrometers, Detectors and Associated Equipment*, vol. 629, no. 1, pp. 93–100, 2011.

[17] S. Torre, T. Antonioli, and P. Benetti, "Study of afterpulse effects in photomultipliers," *Review of scientific instruments*, vol. 54, no. 12, pp. 1777–1780, 1983.

[18] M. Aartsen, K. Abraham, M. Ackermann, J. Adams, J. Aguilar, M. Ahlers, M. Ahrens, D. Altmann, T. Anderson, M. Archinger, *et al.*, "Characterization of the atmospheric muon flux in icecube," *Astroparticle physics*, vol. 78, pp. 1–27, 2016.

[19] R. Dossi, A. Ianni, G. Ranucci, and O. J. Smirnov, "Methods for precise photoelectron counting with photomultipliers," *Nuclear Instruments and Methods in Physics Research Section A: Accelerators, Spectrometers, Detectors and Associated Equipment*, vol. 451, no. 3, pp. 623–637, 2000.